©SNAK, 2012

Hydrodynamic design of an underwater hull cleaning robot and its evaluation

Man Hyung Lee[1], Yu Dark Park[1], Hyung Gyu Park[1], Won Chul Park[2]
Sinpyo Hong[3], Kil Soo Lee[1] and Ho Hwan Chun[4]

[1]*Graduate School of Mechanical Engineering, Pusan National University, Busan, Korea*
[2]*Graduate School of Interdisciplinary Program in Mechatronics, Pusan National University, Busan, Korea*
[3]*Global Core Research Center for Ships and Offshore Plants, Pusan National University, Busan, Korea*
[4]*Department of Naval Architecture and Ocean Engineering, Pusan National University, Busan, Korea*

ABSTRACT: *An underwater hull cleaning robot can be a desirable choice for the cleaning of large ships. It can make the cleaning process safe and economical. This paper presents a hydrodynamic design of an underwater cleaning robot and its evaluation for an underwater ship hull cleaning robot. The hydrodynamic design process of the robot body is described in detail. Optimal body design process with compromises among conflicting design requirements is given. Experimental results on the hydrodynamic performance of the robot are given.*

KEY WORDS: Under water hull cleaning robot; Remotely operated vehicle; Hydrodynamic design.

INTRODUCTION

Hulls of large ships in service need to be periodically cleaned for safety inspections and reduction of drag force. A ship that operates with a clean underwater surface can potentially save over 5% of fuel cost. Hull cleaning also restores effectiveness of antifouling paint and extends the life span of the paint on the hull. Since expensive non-toxic chemicals are currently used for the painting of large ship hulls, the importance of hull cleaning has been growing. However, cleaning of large ships is usually very expensive and inefficient. Cleaning and inspection of ship hulls are usually executed by human divers. There are operational limitations in the cleaning time length and working space for human underwater operations. Thus, an underwater hull cleaning robot (HCR) can be an effective means to reduce economical burden in cleaning and painting of ship hulls.

Compared with cleaning ship hulls in dry docks or on the ground (Iorra et al., 2009), underwater hull cleaning can be economical. The preparation and postprocessing for dry dock cleaning or ground cleaning are quite expensive and time-consuming. Underwater cleaning also increases ship availability.

Underwater HCRs are special types of underwater robots. Underwater robots can be either connected to the surface with tether cables or isolated without tether. There are several types of underwater robots including remotely operated vehicles (ROVs), autonomous underwater vehicles (AUVs), and solar-powered autonomous underwater vehicles (SAUVs). Their application covers exploration of underwater resources, fishing industries, port security, and military operations. The tethered underwater robots are usually called remotely operated vehicles (ROVs). ROVs can take pictures underwater and carry out diverse underwater jobs. The first underwater robot, Pooddle, was developed by a Frenchman Dimitri Rebikoff in 1953 (Marine Technology Society, 2012). In its initial stage of development, United States Navy studied ROV to solve technical problems

---

Corresponding author: *Man Hyung Lee*
e-mail: *mahlee@pusan.ac.kr*

associated with unmanned underwater vehicles (Roberts and Sutton, 2006). The design of an underwater hull cleaning robot was introduced by Yuan et al., 2004. In Korea, ROV research has also been done. (Jung et al., 2009; Jun et al., 2006; Li et al., 2004; Jung et al., 2002; Kim and Shin, 2005).

Even though robots for underwater operations have been actively developed throughout the world, a commercial AUV for underwater hull cleaning has not been introduced. The Office of Naval Research (ONR) of the United States Navy is currently developing an autonomous underwater hull cleaning robot Hull BUG with SeaRobotics Corporation.

The development of underwater hull cleaning robots requires specialized technologies. The robots are supposed to work near the ship hull without damaging the hull paint. Their motions need to have six degrees-of-freedom (DOF) with sub-decimeter accuracy. They demand special propulsion systems to apply wide range of working conditions. They need to cover 2000 m^2/h for inspectional operations and 200 m^2/h for cleaning jobs. The HCR to be considered in this paper is designed to approach the ship from a mother ship or the ground by autonomous navigation. In this paper, 3 m/s has been selected as the practical maximum approaching speed.

While there are many issues in the design of hull cleaning ROV, such as the positions of cleaning brush and metacenter, airproof, keeping of robot's attitude on the inclined hull surface, and anticorrosion (Yuan et al., 2004), important key issues with the development of autonomous underwater HCRs can be related with drag reduction and the design of the positioning system. The main focus in the design of the body is the reduction of body drag to extend the operation period of the cleaning service. Accurate positioning of HCR requires expensive sensor systems, such as long base line (LBL) acoustic positioning system and high grade inertial sensors.

In this paper, the design of the robot body starts from a simple basic model. A comparative study on the fluid dynamic behavior is performed with the basic model and several optional models. From this study, an optimal shape of the body that satisfies the design requirements is determined. Analysis of the flow field around the body is made with computational fluid dynamic (CFD) techniques using turbulence models, standard and RNG $k - \varepsilon$ models. The CFD analysis is performed with the standard $k - \varepsilon$ model. To investigate the influence of turbulence model on the analysis, an additional CFD analysis with the RNG $k - \varepsilon$ model on the optimal shape of the body is executed. Analysis results of the two turbulence models are compared to evaluate the effect of the turbulence model.

BODY DESIGN OF A HULL CLEANING ROBOT

The design of the HCR body involves appropriate compromises between conflicting design goals: mobility and stability, maintenance convenience and stability, and performance and budget. Autonomous navigation of a long path requires stability to overcome large attitude changes induced by external forces such as waves. Thus it is desirable to have a long metacenter, the distance between the centers of gravity and buoyancy. On the other hand, for the robot to clean the sides of the ship hulls, it may be necessary to roll up to 90 degrees and keep its attitude for an extended time. In this case, a short metacenter is advantageous for the large roll motion. If cleaning equipments are installed on the top side of the robot body, it is able to clean the bottom of the hull with only a small change of attitude. The maintenance of cleaning equipments can also be greatly simplified. However, the center of gravity of the body moves downward and stability decreases.

The strategy taken in the design of HCR body is to minimize as much drag reduction as possible. To meet this strategy, a basic model of HCR is designed at first. Then drag forces of the body are computed with various flow speeds. The components that have relatively drags are to be found and their shapes are changed so that the drags on the components are decreased.

General structure of ROV

ROVs can be largely classified as open frame structure or closed frame structure. An ROV with an open frame structure has stable three DOFs motions based on a large metacenter. This type of structure has various additional advantages. This structure is well known and generally adopted by most ROVs. It is convenient for large payloads. Inspection and cleaning equipments can be easily attached to or removed from the body. However, ROVs with this structure have difficulties with motions that require more than three DOFs. Due to these advantages and disadvantages, open frame structure is mainly applied to ROVs for general works.

Even though an ROV with a closed frame structure has potential for greater mobility, it has disadvantages. Due to a short metacenter, it has relatively unstable motions. It also has a small payload. It is very inconvenient in handling large payloads for

Fig. 1 ROVs with open frame structure.

Fig. 2 ROVs with closed frame structure.

cleaning and inspecting. Thus ROVs of closed frame structure are applied to special works that need fast motions.

There are several requirements for HCR. Four DOFs for surge, yaw, heave, and roll are necessary for stable navigation and cleaning works. Attached cleaning brushes can be easily exchanged. Body stability is negligibly affected by the height of the cleaning devices. Finally, maintenance of the body and payload is convenient. Thus, an open frame structure is adopted for the HCR in this study.

In the design of the general arrangement of a ROV, compromise between operational convenience and design complexity is required. The cleaning equipments can be attached to the front side, upper side, left or right sides of the body of HCR. If the equipments are placed on the upper side, HCR is able to clean the bottom of hull with almost the same attitude as when it navigates. It only needs to roll with a considerable angle to clean the sides of the hull. An ROV of this structure is shown in Fig. 3. With this type of structure, the center of gravity tends to move upward making the ROV more unstable. To maintain the center of buoyancy above the center of gravity, an additional payload may be placed at the bottom. The cleaning equipment is placed on the upper side of HCR in this study. Even though the size and weight of ROV can be large, the operational convenience is considered much more important.

Horizontal thrust is used to obtain force to gain horizontal motion. The HCR is required to have horizontal speed of 3 knots. Preliminary estimation of the horizontal speed is made with a simplified body model. The estimated minimum horizontal speed is 3.01 *knots* with the thrust force of 50 *kgf* and drag coefficient of 1.1.
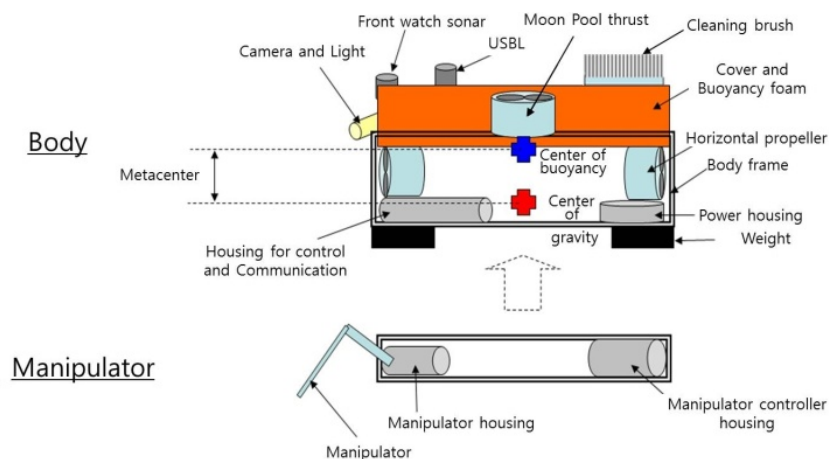

Fig. 3 The structure of HCR.

Vertical thrust is necessary for heave motion. The force is also used to adhere to the surface of the ship hull to be cleaned or to change the roll attitude of HCR. The minimum requirements on the HCR for this study relating to vertical thrust are vertical speed of 1.7 *knots* and roll angle of 90 *degrees*. The HCR has three vertical thrusts. Each thrust has the maximum output of 25 *kgf*. The three thrusts form a triangular shape and the cleaning equipment is placed at the center of the triangle. The maximum roll moment of 18.5 *kgf·m* can be produced with the thrusts. With this arrangement, the vertical thrusts can produce a moment to overcome restoring moment by gravity force when the roll attitude of the body is 90 *degrees*.

The preliminary estimation relating to the vertical thrust verifies that the design requirements can be satisfied with the selected thrusts. The vertical drag force is estimated to be less than 75 *kgf* which is the maximum available vertical thrust force. When the roll attitude of the body is 90 *degrees*, the restoring moment produced by the gravity is 12.09 *kgf·m* which is less than the maximum roll moment of the thrusts.

Design of thrusters

Horizontal thrusters are used for surge and yaw motions of HCR. In order to design the horizontal thrusters to satisfy the requirement of the 3 *knots* of the maximum surge speed, a rough estimation of drag force is calculated using the following relation:

$$F = \frac{1}{2}\rho \cdot C_d \cdot A \cdot V^2 \tag{1}$$

where F is the drag force, ρ is the density of the fluid, C_d is the drag coefficient, A is the frontal area, and V is the velocity of moving object. Assuming that the body shape is a box of rectangular parallelepiped frontal area of 0.28 m^2, the velocity of 3.4 *knots* is obtained in the seawater with the horizontal thrust force of 50 *kgf* and drag force coefficient of 1.1. If a cable drag force of 9.91 *kgf* is added to the body drag force, the speed of 3.01 *knots* is obtained. Thus, the requirement on the maximum surge speed can be satisfied with 50 *kgf* thrust force.

Vertical thrusters are used when HCR moves vertically or changes its roll attitude for cleaning operations. To clean the sides of the ship hulls, 90 *degrees* of the maximum roll angle is necessary. With three thrusters, each has 25 *kgf* thrust force, the HCR can have the maximum vertical speed of 1.7 *knots*. When HCR adheres to the bottom of the hull for cleaning, it can produce the maximum adhesion force of 75 *kgf*. Two of the three vertical thrusters are located as close as possible to the sides of the HCR so that it can produce a large roll moment. It is designed to produce the maximum roll moment of 18.5 *kgf·m* that exceeds the maximum expected restoring moment 12.09 *kgf·m* when the roll angle is 90 *degrees*.

Analysis method

The body of the HCR is designed to minimize the drag force. The computation of the drag force is assisted with computational fluid dynamics (CFD) techniques. Turbulent flow field around the HCR is analyzed with the general CFD analysis code FLUENT/UNS. The governing equations employed in the FLUENT/UNS are the three-dimensional equations for mass and momentum conservations with the standard $k - \varepsilon$ turbulence model. The equation of mass conservation or continuity equation in tensor forms is

$$\frac{\partial \rho}{\partial t} + \frac{\partial (\rho u_j)}{\partial x_j} = 0 \tag{2}$$

where ρ is the specific mass, u_j is the velocity component along the coordinate axis x_j, and t is the time. Assuming incompressible flow, the equation for the momentum conservation is

$$\frac{\partial (\rho u_i)}{\partial t} + \frac{\partial (\rho u_i u_j)}{\partial x_j} = -\frac{\partial p}{\partial x_i} + \frac{\partial \tau_{ij}}{\partial x_j} + \rho g_i + F_i \tag{3}$$

where p is the pressure, g_i is the gravity component along the coordinate axis x_i, F_i is the external force component along the axis x_i, and τ_{ij} is the stress tensor defined as

$$\tau_{ij} = \mu \left(\frac{\partial u_i}{\partial x_j} + \frac{\partial u_j}{\partial x_i} \right) - \frac{2}{3} \mu \frac{\partial u_i}{\partial x_j} \delta_{ij} \tag{4}$$

where μ is the viscosity and δ_{ij}, the Kronecker delta.

Since the flow field around HCR can have turbulence under severe flow conditions, the selection of an appropriate turbulence model may be necessary. In order to analysis the turbulence around a large scale model such as HCR, the standard $k - \varepsilon$ two equation turbulence model that is generally used in industries is considered in this paper. The $k - \varepsilon$ turbulence model is derived from the Reynolds Averaged Navier Stokes (RANS) equations.

$$\frac{\partial (\rho u_i)}{\partial t} + \frac{\partial (\rho u_i u_j)}{\partial x_j} =$$
$$\frac{\partial}{\partial x_j} \left(\mu \left(\frac{\partial u_i}{\partial x_j} + \frac{\partial u_j}{\partial x_i} \right) - \frac{2}{3} \mu \frac{\partial u_i}{\partial x_j} \delta_{ij} \right) - \frac{\partial p}{\partial x_i} + \frac{\partial}{\partial x_j} \left(-\overline{u_i' u_j'} \right) \tag{5}$$

where $\overline{u_i' u_j'}$ is the Reynolds stress due to the random turbulent fluctuations in the fluid momentum. Using the Boussinesq eddy viscosity assumption, the Reynolds stress can be written as

$$-\rho \overline{u_i' u_j'} = \mu_t \left(\frac{\partial u_i}{\partial x_j} + \frac{\partial u_j}{\partial x_i} \right) - \frac{2}{3} \left(\rho k + \mu_t \frac{\partial u_i}{\partial x_j} \right) \delta_{ij} \tag{6}$$

where μ_t is the turbulent viscosity. μ_t can be computed from the turbulent kinetic energy k and turbulent dissipation rate ε as follows:

$$\mu_t = \rho C_\mu \frac{k^2}{\varepsilon} \tag{7}$$

where C_μ is the model constant. The turbulent kinetic energy and turbulent dissipation rate can be obtained from the equations:

$$\frac{\partial (\rho k)}{\partial t} + \frac{\partial (\rho u_i k)}{\partial x_i} = \frac{\partial}{\partial x_i} \left(\left(\mu + \frac{\mu_t}{\sigma_k} \right) \frac{\partial k}{\partial x_i} \right) + G_k + G_b - \rho \varepsilon \tag{8}$$

$$\frac{\partial (\rho \varepsilon)}{\partial t} + \frac{\partial (\rho u_i \varepsilon)}{\partial x_i} =$$
$$\frac{\partial}{\partial x_i} \left(\left(\mu + \frac{\mu_t}{\sigma_\varepsilon} \right) \frac{\partial \varepsilon}{\partial x_i} \right) + C_{1\varepsilon} \frac{\varepsilon}{k} \left(G_k + (1 - C_{3\varepsilon}) G_b \right) - C_{2\varepsilon} \rho \frac{\varepsilon^2}{k} \tag{9}$$

where G_k and G_b are terms due to the turbulent stress and buoyancy, respectively. They can be obtained from the equations as follow:

$$G_k = -\rho \overline{u_i' u_j'} \frac{\partial u_j}{\partial x_i} \tag{10}$$

$$G_b = \beta g_i \frac{\mu_t}{\mathrm{Pr}_t} \frac{\partial T}{\partial x_i} \tag{11}$$

where T is the temperature, Pr_t, the turbulent Prandtl number, and β, the coefficient of thermal expansion. Model constants in equations (8), (9), and (11) are given as follows:

$$\begin{aligned} C_{1\varepsilon} &= 1.44, C_{2\varepsilon} = 1.92, C_\mu = 0.09, \\ \sigma_k &= 1.0, \sigma_\varepsilon = 1.3, \mathrm{Pr}_t = 0.85 \end{aligned} \tag{12}$$

These model constants are obtained from experiments on the basic turbulent shear flows of air and water. To take into consideration of the flow near walls in the standard $k - \varepsilon$ model, turbulence intensity and hydraulic diameter are used in the turbulent specification method. Numerical computations are performed with standard wall function. Analysis algorithm used in FLUENT/UNS is the Semi-Implicit Method for Pressure-Linked Equation (SIMPLE) algorithm of the finite volume method.

Computation of drag force

Since the actual shape of the HCD body is complicated to calculate the drag force, flow field analysis can be easily done by using a simple model of the body. Simple model of the components that have relatively large drag force such as camera, horizontal and vertical thrusts, and roller on the upper side are chosen for easy CFD analysis. Turbulent flow field around the simplified model of the selected components are analyzed with FLUENT.

In order to determine the best shape design of body, the drag force computation is made in two steps. First, a simple basic model is selected and drag force on it is computed. Based on the drag force computation, several options for the shape of the body that may have small drag force are proposed. After the evaluation of the drag force for each option is made, the smallest drag force among the options is chosen as the best option.

Drag force computation on the basic model

The shape of a general ROV is shown in Fig. 4. As shown in the figure, the structures of the inside and lower part of the body are quite complicated. The thin frames that connect the upper and lower structures may have relatively small drag forces.
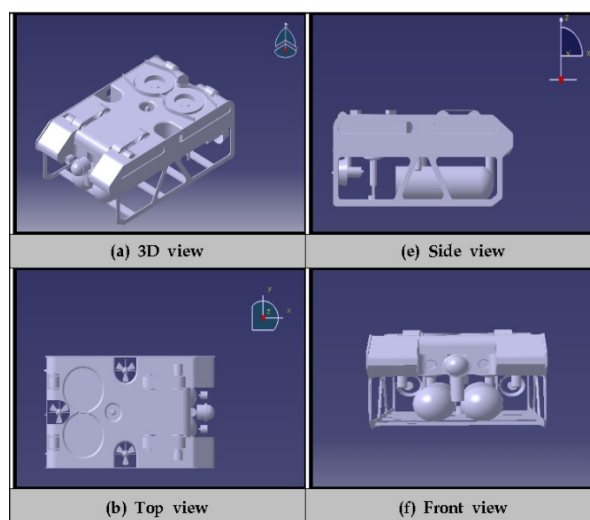

Fig. 4 The shape of a general ROV.

However, they require large time for the generation of mesh around them for CFD analysis and may cause uncertainties on the CFD analysis results due to their undesirable effects on the overall mesh quality. Therefore, simple forms of the upper and lower structures that have major effect on the drag force are derived for the basic model of HCR. Fig. 5 shows the basic model.
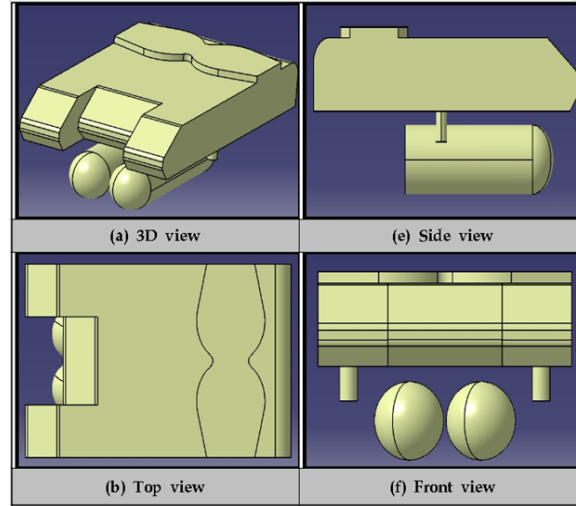

Fig. 5 The shape of basic model.

The mesh for the flow analysis with the basic model is generated as follow. An unstructured triangle mesh is generated by running Gambit v.2.3.16. The mesh size is 0.5 near the HCR body. The size increases with the distance from the body. To decide the proper number of mesh elements, the tests of the dependency on the element number are conducted. 150 million mesh elements are chosen after testing 80 million, 150 million, and 200 million mesh elements. The details of the test results was omitted in consideration of paper's length.

The computation region and boundary conditions are roughly shown in Fig. 6. Let the length of HCR in the flow direction be L. Then the length from the inlet to the front of the body is $4L$, the length from the rear of the body to the outlet is $8L$, and both the height and width of the computation region are $4L$. The inlet condition is determined by the flow speed. Outlet conditions are given on the convection and vertical and horizontal planes of symmetry. Viscosity conditions are given on the surface of the HCR.

The drag force is computed in the steps of 0.5 *knots* flow speeds in the range of 0-5 *knots*. Drag force can be written as

$$F_T = F_p + F_V \tag{13}$$

where F_T is the total drag force, F_p, the pressure or form resistance, and F_V, the viscous resistance. Thus, considering equation (1), the drag coefficients can be written as

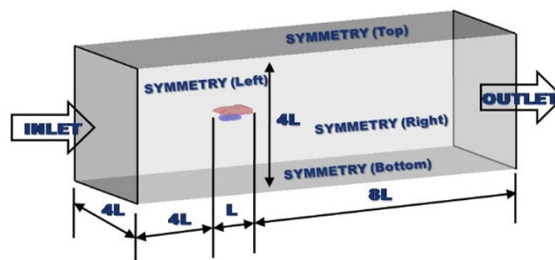$$C_D = \frac{2F_T}{\rho U^2 A}, C_{DP} = \frac{2F_P}{\rho U^2 A}, C_{DV} = \frac{2F_V}{\rho U^2 A} \tag{14}$$

Fig. 6 Computation region and boundary conditions.

where U is the inlet flow velocity, ρ is the fluid density, and A is the frontal area. As shown in Table 1, the drag force computation results show that pressure resistance is dominant and the effect of viscous resistance is quite weak. Total drag force is 9.3 *N* with the flow speed of 0.5 *Knots*. The drag increases in a parabolic shape as the flow speed increases. The maximum drag force is 911 *N* at the maximum speed of 5 *Knots*. The drag coefficient shows similar values for the speed range with the variation less than 1 % as shown in Fig. 7. In order to derive optimum body shape, the pressure resistance of each component of HCR body is computed to conclude which component has the major influence on the drag.

Table 1 Drag forces and coefficient with flow speeds.

| Velocity (*Knot*)	$F_P(N)$	$F_V(N)$	$F_T(N)$	C_{DP}	C_{DV}	C_D
0.5	8.24956	1.07466	9.32422	0.59164	0.07707	0.66872
1.0	33.13114	3.82893	36.96008	0.59403	0.06865	0.66268
1.5	74.70490	8.09883	82.80373	0.59520	0.06545	0.65984
2.0	132.99836	13.81142	146.80978	0.59615	0.06191	0.65806
2.5	208.02904	20.91993	228.94897	0.59678	0.06001	0.65679
3.0	299.81985	29.39068	329.21052	0.59729	0.05855	0.65584
3.5	408.35072	39.19628	447.54699	0.59768	0.05737	0.65505
4.0	533.65909	50.31608	583.97516	0.59802	0.05639	0.65440
4.5	675.74219	62.73170	738.47388	0.59831	0.05554	0.65385
5.0	834.60425	76.42770	911.03194	0.59856	0.05481	0.65337
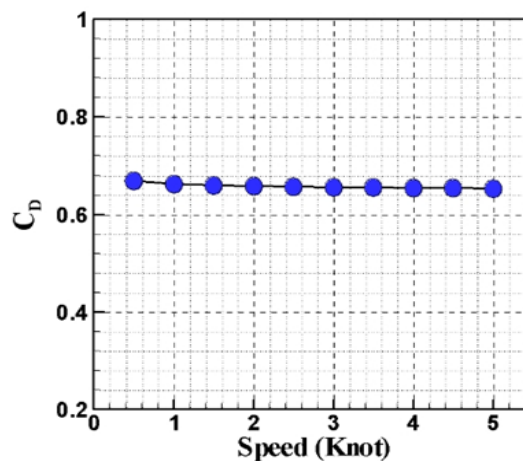
Fig. 7 Total drag coefficient.

Surface pressure distribution and flow pattern for the basic model

In order to find the shape of HCR body that has low pressure resistance, pressure distribution on the surface of the basic body model is analyzed. The components that have relatively large positive or negative pressure are found. Fig. 8 shows the pressure distribution on the body surface with the maximum flow speed 3 *Knots* from various view angles. It shows the stagnation points at the front of parts 1, 3, and 4 have relatively high pressures. In the case of housing, part 4, the shape of the

front parts are hemispheres and the area with high pressure is relatively small. This shape has a desirable pressure distribution such that the pressure has the maximum value at the center and decreases as the distance from the center increases.

Fig. 9 shows flow patterns around the basic model. The cross sections in the figure are defined in Fig. 8. Cross section 1 is the transverse section that cuts through the center of the model. Cross sections 2 and 3 are the transverse sections that cut through the center of housing and a vertical thruster, respectively. Cross section 4 is the longitudinal section to watch the wake distribution at the front part of the horizontal thrusters.

The flow patterns around upper and lower structures are very similar to those around blunt objects. A stagnation point is generated at the front part of each structure. The flow accelerates after the stagnation point until the point of inflection. There is no large vortex around the front part of the model. However, it can be seen that there are relatively large vortices around the rear part of the model. There are also small vortices in the wakes of cleaning brushes on the upper side and vertical thrusters on the lower side of the model. The areas which generate vortices have relatively large magnitude of negative pressures.
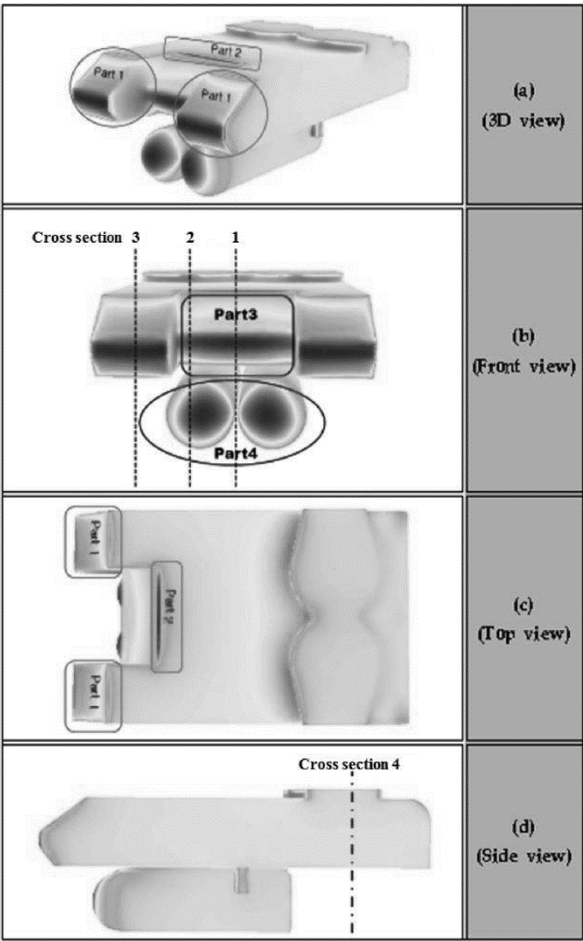

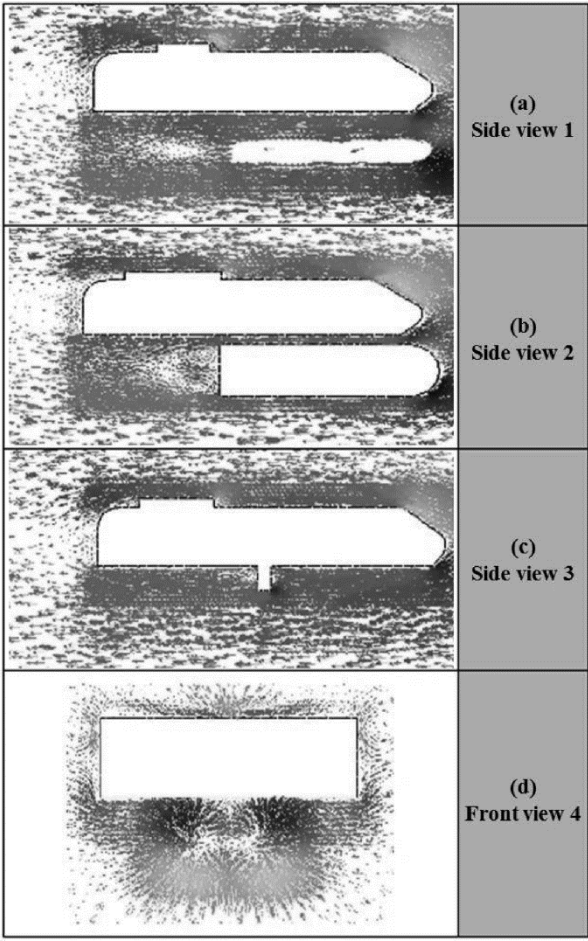Fig. 8 Pressure distribution on the basic
HCR body model surface.

Fig. 9 Flow pattern around the basic
HCR body model.

Design of the final model with small resistance

With small modifications on the basic model, a new model that has small drag will be designed. The arrangement of equipments is unchanged and the shape of each component that has large resistance will be changed. The previous analysis results on the pressure distribution and flow pattern show that parts 1, 3, and 4 have relatively large resistance. To reduce resistance, each shape of the parts is changed to have streamlined form.

Several optional models of the HCR body that have streamlined forms are selected and resistances are analyzed as before. A

comparative study on the resistance analysis on the optional models is conducted and a final model is decided that has the smallest drag based on the resistance analysis results. Fig. 10 shows the shapes of basic and final models seen from various view angles. The front areas of parts 1 and 3 and rear area of part 4 in the final model are more streamlined compared with those of the basic model. The details of the new model are omitted with the consideration of paper size.
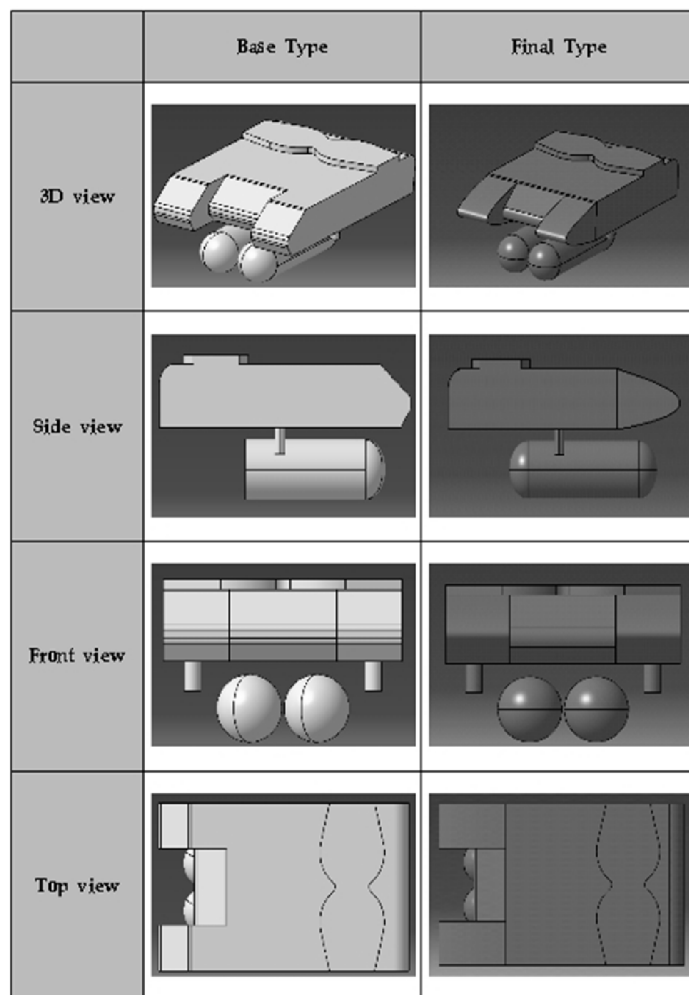

Fig. 10 The shapes of basic and final models.

Table 2 shows the drag force analysis results on the basic and final models with various flow speeds. The table shows that hemisphere form of lower rear part reduces drag force by six percent compared with the initial simple basic model. It is also found that eleven percent drag force reduction can be obtained by streamlining the bow part of the upper structure. The overall drag on the HCD can be reduced by seventeen percent with optimized body shape.

In this paper the standard $k-\varepsilon$ turbulence model is used for the flow field analysis because the model is most generally considered in industries to analyze turbulent flow fields around large scale models. However, the standard model is not able to simulate the series of vortices generated by flow separation. The RNG $k-\varepsilon$ is used to overcome the drawbacks of the standard $k-\varepsilon$ model. Thus, the vortices generated after blunt objects can be simulated with the RNG $k-\varepsilon$ model. In order to evaluate the effect of turbulence model, the drag force computations on the HCR body models are conducted using RNG $k-\varepsilon$ model with the mesh system similar to that used in the standard $k-\varepsilon$ model. Table 3 shows drags and drag coefficients for the basic and final models with the two turbulence models when the flow velocity is 3 *Knots*. Even though the values of drag forces are different from each other for the two turbulence models, the drag force reduction ratios are quite similar.

Table 2 Drags and drag coefficients for the basic and final models.

Velocities (*Knot*)	Base Type		Final Type	
	$F_T(N)$	C_D	$F_T(N)$	C_D
0.5	9.32422	0.66872	7.8138864	0.56039717
1.0	36.96008	0.66268	30.726745	0.55091599
1.5	82.80373	0.65984	68.540203	0.54617486
2.0	146.80978	0.65806	121.23236	0.54340975
2.5	228.94897	0.65679	188.75908	0.54149777
3.0	329.21052	0.65584	271.09933	0.54007589
3.5	447.54699	0.65505	368.22991	0.53895415
4.0	583.97516	0.65440	480.14197	0.53804492
4.5	738.47388	0.65385	606.802	0.53726781
5.0	911.03194	0.65337	748.22128	0.53661016

Table 3 Drags and drag coefficients with different turbulence models (Velocity: 3 *Knots*).

Case	Standard k-ε model			RNG k-ε model		
	$F_T(N)$	C_D	Drag reduction ratio (%)	$F_T(N)$	C_D	Drag reduction ratio (%)
Base model	329.210	0.656	17.65	286.604	0.571	18.96
Final Model	271.099	0.540		232.273	0.463	

Construction of HCR body

The arrangement of major parts of the body requires compromise between the performance of angular motion and that of translational motion. For the stable angular motion with small thrust, short distance between the center of gravity and the center of buoyancy, is desirable. However, for stable navigation with translation motion, long distance between them is necessary. The body parts of HCR is arranged so the metacenter is as long as possible to satisfy the angular motion requirements.

Fig. 11 Pictures of HCR seen from various view angles.

Based on the shape design and arrangement of body detail, the design is made. If the proposed shape or arrangement cannot be satisfied during the detail design, the shape or arrangement is modified and the detail design is processed again. Material selection, structural stability analysis, machining methods, detail dimension such as thickness and length, and thermal analysis are made for the detail design. Fig. 11 shows the final HCR taken from various view angles.

EXPERIMENTS ON THE HYDRODYNAMIC PERFORMANCE OF HCR

More tests may be necessary to verify the performance of HCR. However, tests that are directly related to the hydrodynamic performance of HCR such as drag force and speed are presented in this paper.

Experiments on the body drag force

In order to examine the drag force of the HCR body, tests are conducted in a towing tank. HCR is towed by a towing carriage at speeds from 0 to 4 *Knots* and drag force is measured by a resistance dynamometer. The shape of the strut to connect the HCR body with resistance dynamometer is streamlined to reduce drag force on the submerged part. During the tests, floats and weights are added inside the HCR body to change the centers of gravity and buoyancy so that the transverse and longitudinal trims are minimized. The required magnitude of the horizontal thrust force to run with the target maximum speed can be determined from the drag force measurements.

The tests for drag force measurement are conducted with seven discrete speeds from 0 to 2.1 *m/s* at a regular interval, 0.3 *m/s*. Three measurements are obtained for each speed. The drag coefficients are obtained with the drag measurements using the equation (1) where the frontal area of the HCR is 0.670 *m²*. The resistance dynamometer used in the drag tests can measure up to 3,000 *N*. Its accuracy is 0.2 % of the full scale. The dynamometer is calibrated with a standard dynamometer whose maximum force range is 5,000 *N* and accuracy 0.03 % of the full scale. Fig. 12 and 13 show the resistance dynamometer and side views of HCR mounted on the carriage, respectively.
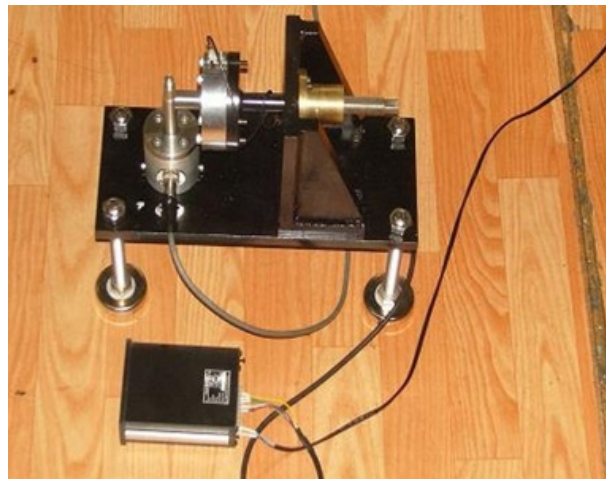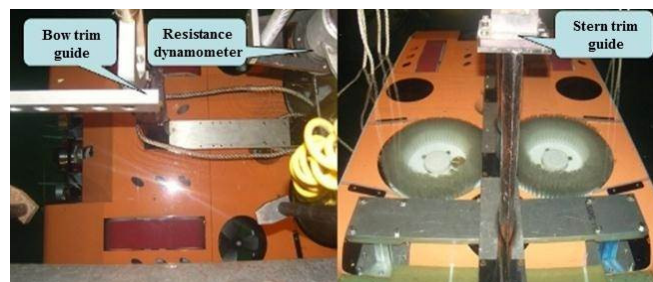

Fig. 12 Resistance dynamometer.

Fig. 13 Side views of HCR mounted on the carriage.

Table 4 Drag measurement results.

1st Trial				
Velocity (*m/s*)	Total resistance F_T (*N*)	Strut resistance F_S (*N*)	HCR resistance F_D (*N*)	Drag coefficient C_D
0.0	0.0000	0.0000	0.0000	0.0000
0.3	26.0935	1.1121	24.9815	0.8302
0.6	99.4686	2.6913	96.7773	0.8041
0.9	225.9598	5.2725	220.6872	0.8149
1.2	400.1130	5.1324	394.9806	0.8204
1.5	509.4221	6.6479	502.7742	0.6684
1.8	742.3665	9.7201	732.6464	0.6764
2.1	889.0749	14.0249	875.0500	0.5935
2nd Trial				
Velocity (*m/s*)	Total resistance F_T (*N*)	Strut resistance F_S (*N*)	HCR resistance F_D (*N*)	Drag coefficient C_D
0.0	0.0000	0.0000	0.0000	0.0000
0.3	27.5458	1.1121	26.4338	0.8785
0.6	111.0022	2.6913	108.3109	0.8999
0.9	234.8187	5.2725	229.5461	0.8476
1.2	368.8709	5.1324	363.7385	0.7555
1.5	501.4406	6.6479	494.7927	0.6578
1.8	651.3177	9.7201	641.5976	0.5923
2.1	906.0459	14.0249	892.0210	0.6050
3rd Trial				
Velocity (*m/s*)	Total resistance F_T (*N*)	Strut resistance F_S (*N*)	HCR resistance F_D (*N*)	Drag coefficient C_D
0.0	0.0000	0.0000	0.0000	0.0000
0.3	28.9755	1.1121	27.8634	0.9260
0.6	113.8630	2.6913	111.1716	0.9237
0.9	233.0049	5.2725	227.7323	0.8409
1.2	336.7526	5.1324	331.6202	0.6888
1.5	450.7082	6.6479	444.0603	0.5903
1.8	822.0404	9.7201	812.3203	0.7499
2.1	951.5357	14.0249	937.5107	0.6359

Table 4 and Figs. 14 and 15 show HCR drag measurement results. The relationship between the drag force and velocity can be described with the second order polynomial

$$y = 156.1x^2 + 112.0x - 9.505 \tag{15}$$

where x is the velocity in *m/s* and y is the drag force in *N*. The measured average drag coefficients are distributed between 0.60 and 0.83. For each velocity, the measured drag forces show small differences. These differences can be due to the trim changes in the tests. The average values of drag force and drag coefficient measurements are larger than those obtained from CFD. The reason for these discrepancies can be considered to be the result of the setups for the experiments and CFD are quite different from each other.
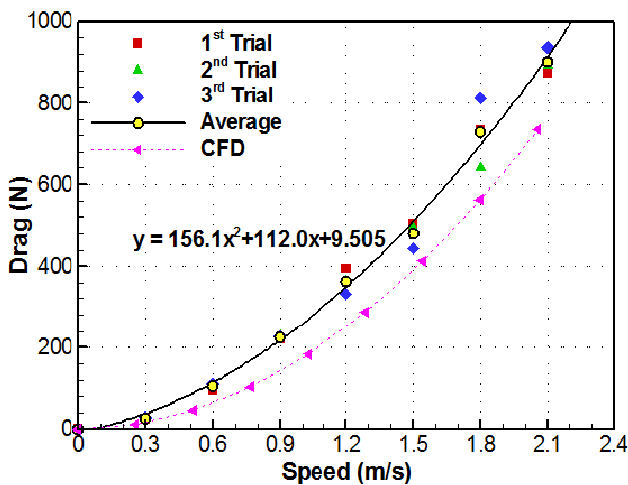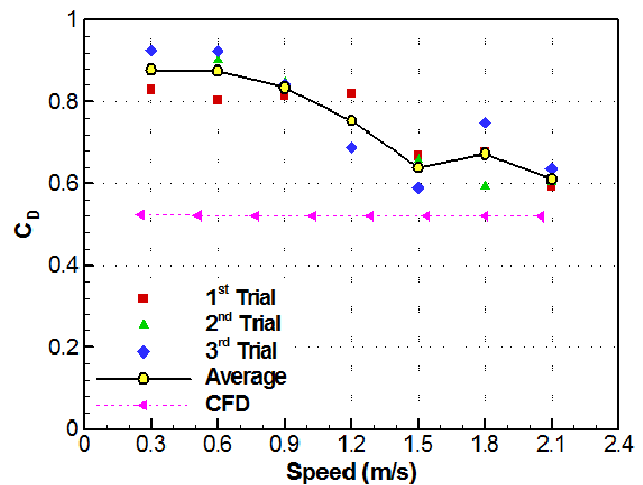

Fig. 14 Drag measurements.

Fig. 15 Drag coefficient.

Experiments on the forward velocity

The tests on the horizontal speed of HCR are conducted with five levels of speed. The forward speed of HCR is measured with two methods. The speed is determined by an electromagnetic flow meter or by the time of travel for a predetermined distance. The flow meter is attached to the bottom side of the HCR body.

During the tests, HCR navigates freely near the surface of the water with neutral buoyancy. The accuracy of the electromagnetic flow meter used in the experiments is 2 % of full scale or ± 0.005 *m/s*. Fig. 16 shows the electromagnetic flow meter used in the tests. The flow meter attached on the bottom side of HCR is shown in Fig. 17.

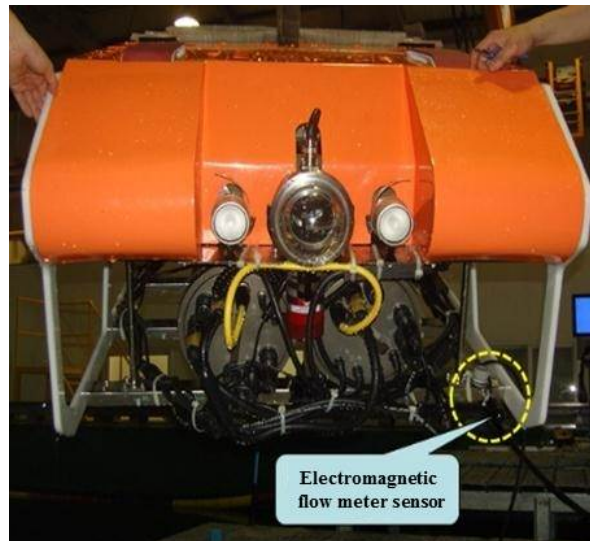Fig. 16 Electromagnetic flow meter used in the speed measurements.

Fig. 17 Electromagnetic flow meter installed on HCR.

The speed commands for the velocity test have discrete values from 0 to full range at the regular interval, one fifth of the full range. The test consists of three sets of experiments. During each set of experiments, HCR velocities are measured for the velocity commands increasing from 0 to the full range. Average velocity for a given velocity command is derived from the elapsed time to travel 10 *m* distance. The instantaneous maximum and minimum velocities obtained from the flow meter is used to determine measurement deviations. The measurement deviation is defined as the half of the difference between the maximum and minimum values.

Table 5 and Fig. 18 show the velocity test results. It shows the maximum velocity is 1.016 *m/s* for the maximum velocity command. The relation between velocity measurement sand commands can be described with the linear equation

$$y = 1.09x - 0.094 \tag{16}$$

where x is the velocity command and y is the velocity measurement in *m/s*. During velocity tests, HCR moves along a relatively straight line in the forward direction. Thus, it can be considered that the direction of the forward thrust force is appropriately adjusted and the weight distribution of HCR body is well balanced.

Table 5 Forward speed with main thrusters.

| Velocity Commands	Velocity (*m/s*)						Averaged Velocity	
	1st Trial		2nd Trial		3rd Trial			
	Mean	Deviation	Mean	Deviation	Mean	Deviation	Mean	Deviation
0/5	0.000	0.000	0.000	0.000	0.000	0.000	0.000	0.000
1/5	0.013	0.003	0.013	0.003	0.013	0.003	0.013	0.003
2/5	0.310	0.060	0.385	0.115	0.375	0.105	0.357	0.093
3/5	0.450	0.050	0.551	0.065	0.512	0.075	0.505	0.063
4/5	0.725	0.175	0.846	0.200	0.871	0.250	0.814	0.208
5/5	0.990	0.040	1.002	0.250	1.055	0.165	1.016	0.152
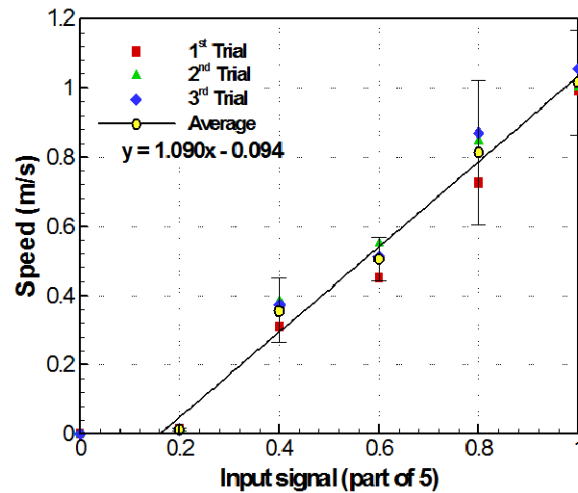
Fig. 18 Forward speed with main thrusters.

Experiments on the vertical thrust

The test for the vertical thrust force measurement is conducted in the towing tank. A commercial weighing scale with 300 *kg* capacity and 0.1 *kg* accuracy is used to measure the thrust force. The scale hangs down from a ceiling hoist and the HCR hangs down from the scale. Discrete input commands from 0 to the full range at the resolution, one eighth of the full range, are sent to the vertical thrusters. Due to the hysteresis symptom in the scale, only one measurement is taken for each command input. For a given command input, the mean value of vertical thrust force is defined as the half of the sum of the maximum and minimum values of the weighting scale measurements. The deviation of thrust force is defined as the half of the difference between the maximum and minimum values of the measurements. Fig. 19 shows the weighting scale for the vertical thrust force measurement.

Fig. 19 The weighting scale for vertical thrust force measurement.

Table 6 and Fig. 20 show the experimental results of the vertical thrust force measurement. During the test, only two vertical thrusters near both sides of HCR are used. With the two thrusters, sufficient roll moment can be generated to maintain 90 *degree* roll attitude. The maximum thrust force 41.5 *kgf* is obtained with the maximum thrust command input. It can be seen that the thrust force reaches nearly its maximum with one quarter of full command input.

Table 6 Experimental results of vertical thrust test.

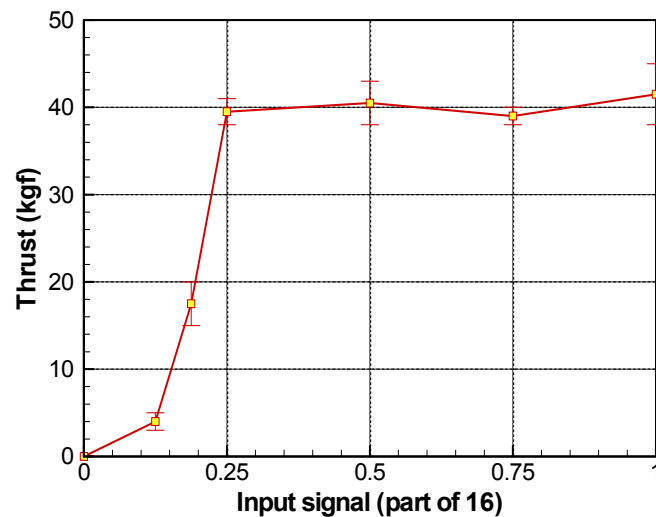| Command input	Vertical thrust force (*kgf*)	
	Mean	Deviation
0	0.0	0.1
1/8	4.0	2
3/16	17.5	5
4/16	39.5	3
8/16	40.5	5
12/16	39.0	2
1	41.5	7

Fig. 20 Vertical thrust force measurements.

CONCLUSIONS

The design of HCR body requires compromises among conflicting requirements. Tradeoffs may be necessary between stability and mobility. A compromise between operational convenience and design complexity is also necessary. From these considerations, an open frame ROV that has a cleaning brush on the top side is selected as the structure of HCR.

The robot body design is optimized to reduce drag force. CDF analysis results reveal that drag due to pressure difference is dominant and the influence of viscosity on it is negligible. An extensive analysis on the flow field around the robot body with CFD suggest that a significant reduction in the drag force can be obtained by adopting hemisphere form of lower rear part and streamlined form of the bow part of upper structure.

The influence of turbulence is included with $k-\varepsilon$ model in the CFD analysis. Most of the CFD analysis is conducted with the standard $k-\varepsilon$ model. To investigate the influence of turbulence model on the drag analysis, additional analysis with the RNG $k-\varepsilon$ model on the final HCR body model is conducted. It is shown that both the standard and RNG $k-\varepsilon$ turbulence models produce similar trends in the drag analysis. The comparison of the drag fore reduction ratio of the two turbulence models may not be justified to use $k-\varepsilon$ model for flow field analysis. For in-depth analysis, comparisons of the analysis results of drag force reduction ratio distribution over speed and characteristics of vortices may be necessary as a further research.

Experiments are conducted to inspect on the hydrodynamic performance of the robot. The results show that the measurements of the drag force are larger than that obtained from the CFD analysis. This discrepancy is considered to be the different setups for the CFD analysis and actual test. Thus, the measured maximum forward velocity is below the target velocity.

ACKNOWLEDGEMENT

REFERENCES

Iorra, A., Caceres, D., Oritz, E., Franco, J., Palma, P. and Alvarez, B., 2009. Design of service robots. *IEEE Robotics & Automation Magazine*, 16(1), pp.24-33.

Jung, K.Y., Kim, I.S., Yang, S.Y. and Lee, M.H., 2002. Autopilot design of an autonomous underwater vehicle using ro-bust control. *Transaction on Control Automation, and Systems Engineering*, 4(4), pp.264-269.

Jun, B.H., Lee, J.H. and Lee, P.M., 2006. Repetitive periodic motion planning and directional drag optimization of under-water articulated robotic arms. *International Journal of Control, Automation, and Systems*, 4(1), pp.42-52.

Jung, Y.S., Lee, K.W., Lee, S.Y., Choi, M.H. and Lee, B.H., 2009. An efficient underwater coverage method for multi-AUV with sea current disturbances. *International Journal of Control, Automation, and Systems*, 7(4), pp.615-629.

Kim, H.S. and Shin, Y.K., 2005. Design of adaptive fuzzy sliding mode controller based on fuzzy basis function expansion for UFV depth control. *International Journal of Control, Automation, and Systems*, 3(2), pp.217-224.

Li, J.H., Lee, P.M. and Jun, B.H., 2004. A neural network adaptive controller for autonomous driving control of an auto-nomous underwater vehicle. *International Journal of Control, Automation, and Systems*, 2(3), pp.374-383.

Marine Technology Society, 2012. *ROVs-A BRIEF HISTORY*. [Online] Available at: <http://www.rov.org/rov_history.cfm> [Accessed 19 November 2012].

Roberts, G. and Sutton, R., 2006. *Advances in unmanned marine vehicles*. IEE, London.

Yuan, F.-C., Guo, L.-B., Meng, Q.-X. and Liu, F.-Q., 2004. The design of underwater hull-cleaning robot. *Journal of Ma-rine Science and Applications*, 3(1), pp.41-45.